Springer

KSME

Journal of Mechanical Science and Technology 33 (6) (2019) 2573~2586
www.springerlink.com/content/1738-494x(Print)/1976-3824(Online)
DOI 10.1007/s12206-019-0505-9

An enhanced multipoint optimal minimum entropy deconvolution approach for bearing fault detection of spur gearbox †

Yuanbo Xu[1], Zongyan Cai[1,*], Xiaoyan Cai[2] and Kai Ding[1]

[1]*School of Mechanical Engineering, Chang'an University, Shaanxi 710064, China*
[2]*School of Economics and Management, Chang'an University, Shaanxi 710064, China*

(Manuscript Received September 18, 2018; Revised December 9, 2018; Accepted February 22, 2019)

Abstract

Previous research has shown that minimum entropy deconvolution (MED) is an effective technique for detecting impulse-like signals, such as the bearing fault and gear fault signals. However, some problems still exist in this technique. With the aim of overcoming these limitations, in this paper, an enhanced MED called multipoint optimal minimum entropy deconvolution adjusted (MOMEDA) is proposed. MOMEDA can succeed in detecting multiple impulses. Unfortunately, according to some simulations and real tests in this work, the results of applying this technique to the fault signals directly were grudgingly acceptable but not very satisfactory, especially under a harsh working condition. This means that MOMEDA is a little sensitive to intensive background noise and vibration interference. To overcome this drawback, a novel mode decomposition method, named time-varying filtering for empirical mode decomposition (TVF-EMD), is applied to adaptively eliminate background noise and vibration interference prior to using MOMEDA. According to this proposed method, the weak bearing fault features can be identified clearly. The proposed approach is utilized in bearing fault detection of a spur gearbox and the results show its superiority and effectiveness.

Keywords: Bearing fault detection; Empirical mode decomposition; Time varying filter; Multipoint optimal minimum; Entropy deconvolution

1. Introduction

The ball bearing, though a vital element of mechanical systems, often gives rise to catastrophic failures. Hence, to avoid unnecessary accidents and losses, the condition monitoring of bearings is indispensable.

Fortunately, with the development of the non-linear and non-stationary signal processing techniques, bearing fault signals have been extensively studied and a range of effective detection tools are now available. Many of the popular bearing fault extraction methods have been presented, including wavelet-based methods [1-3], spectral kurtosis and entropy [4-6], mode decomposition-based methods [7-10], independent cmponent analysis methods (ICA) [11, 12] and intelligent and optimization algorithms [13-18].

When a failure occurs in the outer or inner rings of a bearing, periodical impulsive components will appear in the fault signals, and these impulses generally carry useful and important information [19]. However, numerous vibration signals measured from mechanical systems are severely corrupted by the noise and interfering components in the transmission paths from the vibration sources to the transducer [20]. Namely, the measured vibration signals usually contain inevitable noise of background and vibration interfering components. Since the periodical impulses are weak signals, they are easily submerged by noise and interfering components emanating from complex mechanical systems. Consequently, the main challenge is how to detect the weak periodical impulses from the complex working environment.

The minimum entropy deconvolution (MED) technique is specially designed to address this issue, which can reconstruct the impulse-like signals similar to the raw impulse signals. MED was first designed by Wiggins [21] in 1978 to process the measured seismic signals and the author successfully obtained impulse-like signals. Realizing that many of mechanical fault signals are similar to the seismic signals, MED was first applied by Endo et al. [22] to detect the gear tooth fault signatures. Due to its effectiveness in fault diagnosis, multiple studies in recent years have focused on this powerful technique [23-25]. Although these studies have provided a wealth of remarkable results with MED on machine fault detection, some of the crucial issues that are most important for a complete application of MED remain unanswered. There are three central drawbacks as follows:

(1) MED only extracts a single impulse instead of multiple

*Corresponding author. Tel.: +86 2982334586, Fax.: +86 2982334588
E-mail address: czyan@chd.edu.cn
† Recommended by Associate Editor Kyoung-Su Park

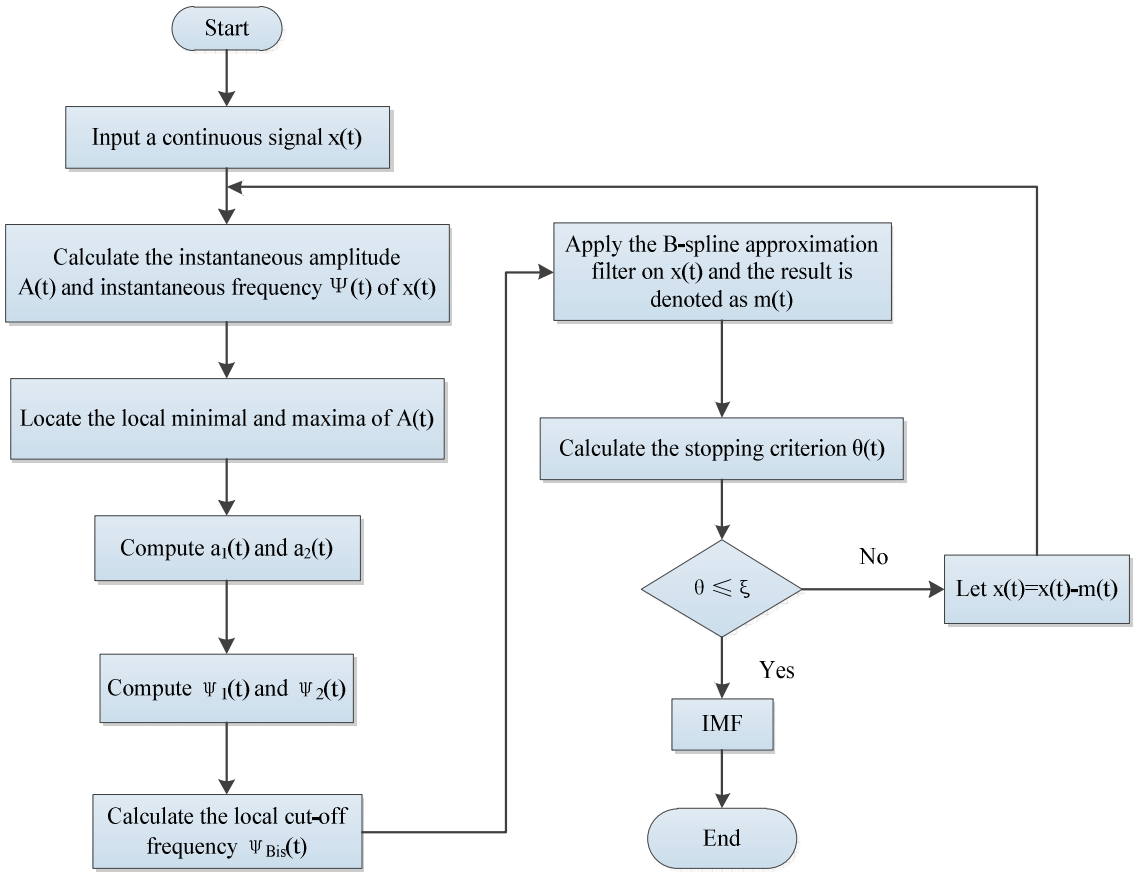

Fig. 1. Flowchart of TVF-EMD.

impulses in most cases;

(2) MED is an iterative approach and thus iterative parameters have to be determined.

(3) Although MED can offer an appropriate solution to the maximization problem, this solution is not necessarily optimal.

To deal with the shortcomings, a novel deconvolution technique, called multipoint optimal minimum entropy deconvolution adjusted (MOMEDA) was proposed by McDonald in 2017 [26]. Using MOMEDA, the position of the impulsive components derived from deconvolution can be defined by a time target vector. Additionally, an optimal solution can be provided for the filter banks with a non-iterative way directly. Meanwhile, MOMEDA can avoid a resampling stage as it is able to work with non-integer fault periods. Based on these advantages, Wang et al. [27] used this method to detect compound faults extraction of a gearbox successfully. However, they reported that MOMEDA cannot precisely extract the fault period signals under a heavy noisy environment. Actually, the same phenomenon appears in our work. The raw vibration signals, therefore, need to be pre-filtered prior to using MOMEDA. Wang et al. [27] used MED to suppress the background noise and then applied MOMEDA to identify the multiple weak impulses from the MED denoised signals. However, as mentioned previously, MED still has some problems unresolved. Consequently, a self-adaptive denoising method is a wise choice.

It is well known that mode decomposition techniques resemble a filter bank [28, 29]. Nevertheless, the existing mode decomposition techniques, more or less, have some shortcomings. For example, empirical mode decomposition (EMD) still has an evident drawback unresolved, i.e., the mode mixing, especially in the presence of the signal with intermittent oscillation. Another improved mode decomposition tool called variational mode decomposition (VMD) is more robust in processing the signal than EMD, but, like MED, the selection of the parameters in VMD may determine its performance, which may impede its application in industries.

Most recently, an improved mode decomposition technique based on empirical mode decomposition (EMD) was proposed by Li et al. [30]. This new mode decomposition technique combines time-varying filtering with EMD. Although TVF-EMD was developed on the basis of EMD, it can perfectly cope with the mode mixing in the EMD technique. Besides, the TVF-EMD method can still remain robust when the sampling rate is lower. Finally, unlike VMD, the predefined parameters in TVF-EMD do not exert a strong influence on results, so it is a fully adaptive data analysis technique [30, 31].

Hence, according to the previous analysis, an enhanced bearing signature detection approach based on MOMEDE and TVF-EMD is presented in this paper. The remaining sections

of this paper are arranged as follows: the principles of TVF-EMD and MOMEDA are described in Secs. 2 and 3, respectively. Secs. 4 and 5 mainly validate the superiority of this proposed method through simulated and real tests. The brief conclusions are located in the last section.

2. TVF-EMD technique

The principle of TVF-EMD is easy to understand, whose procedure is summarized in following three steps: (1) Look for the local cut-off frequency, (2) obtain the local mean by using the (time-varying filtering) TVF, and (3) check if the residual component satisfies the stopping criterion. The flowchart of the TVF-EMD is shown in Fig. 1. For a detailed procedure of this technique, interested readers can refer to Ref. [28].

3. MOMEDA

3.1 Principle

MOMEDA is tailored to detect bearing fault signatures featuring multiple impulses instead of a single impulsive component. This maximization problem as multipoint optimal minimum entropy deconvolution adjusted (MOMEDA) is defined:

$$\text{Multi D-Norm} = \text{MDN}\left(\vec{y},\vec{t}\right) = \frac{1}{\|\vec{t}\|}\frac{\vec{t}^{T}\vec{y}}{\|\vec{y}\|}, \tag{1}$$

$$\text{MOMEDA:}\ \max_{f}\ \text{MDN}\left(\vec{y},\vec{t}\right) = \max_{f}\frac{\vec{t}^{T}\vec{y}}{\|\vec{y}\|}, \tag{2}$$

in which the target vector $\vec{t}$ denotes a constant vector that determines the weightings and position of the impulsive components.

The extremes of Eq. (2) are calculated by taking the derivative with respect to the filter coefficients, $\vec{f} = f_1, f_2, ..., f_L$:

$$\frac{d}{d\vec{f}}\left(\frac{\vec{t}^{T}\vec{y}}{\|\vec{y}\|}\right) = \frac{d}{d\vec{f}}\left(\frac{t_1 y_2}{\|\vec{y}\|}\right) + \frac{d}{d\vec{f}}\left(\frac{t_2 y_2}{\|\vec{y}\|}\right) + ... + \frac{d}{d\vec{f}}\left(\frac{t_{N-L} y_{N-L}}{\|\vec{y}\|}\right). \tag{3}$$

Since:

$$\frac{d}{d\vec{f}}\left(\frac{t_k y_k}{\|\vec{y}\|}\right) = \|\vec{y}\|^{-1} t_k \vec{M}_k - \|\vec{y}\|^{-3} t_k y_k X_0 \vec{y}, and \vec{M}_k = \begin{bmatrix} x_{k+L-1} \\ x_{k+L-2} \\ \vdots \\ x_k \end{bmatrix} \tag{4}$$

Thus Eq. (4) can be expressed:

$$\frac{d}{d\vec{f}}\left(\frac{\vec{t}^{T}\vec{y}}{\|\vec{y}\|}\right) = \|\vec{y}\|^{-1}\left(t_1\vec{M}_1 + t_2\vec{M}_2 + ... + t_{N-L}\vec{M}_{N-L}\right) - \|\vec{y}\|^{-3}\vec{t}^{T}\vec{y}X_0\vec{y} \tag{5}$$

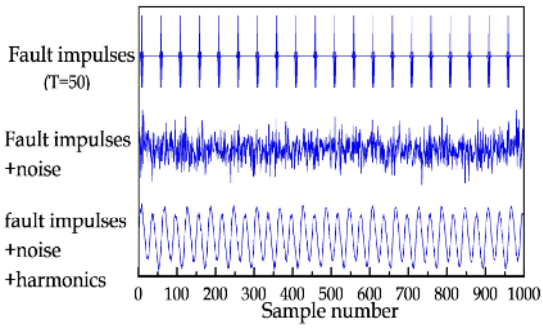

Fig. 2. Simulated fault signal.

We can simplify as follows:

$$t_1\vec{M}_1 + t_2\vec{M}_2 + ... + t_{N-L}\vec{M}_{N-L} = X_0\vec{t}, \tag{6}$$

and compute for extremes by equating to $\vec{0}$ Eq. (6) can be found to be

$$\|\vec{y}\|^{-1} X_0\vec{t} - \|\vec{y}\|^{-3}\vec{t}^{T}\vec{y}X_0\vec{y} = \vec{0}, \tag{7}$$

$$\frac{\vec{t}^{T}\vec{y}}{\|\vec{y}\|^2} X_0\vec{y} = X_0\vec{t}. \tag{8}$$

Since $\vec{y} = X_0^{T}\vec{f}$ and assuming $\left(X_0X_0^{T}\right)^{-1}$ exists

$$\frac{\vec{t}^{T}\vec{y}}{\|\vec{y}\|^2}\vec{f} = \left(X_0X_0^{T}\right)^{-1} X_0\vec{t}. \tag{9}$$

The optimal filter bank and output solutions are computed as follows:

$$\vec{f} = \left(X_0X_0^{T}\right)^{-1} X_0\vec{t}. \tag{10}$$

$$X_0 = \begin{bmatrix} x_L & x_{L+1} & x_{L+2} & \cdots & \cdots & x_N \\ x_{L-1} & x_L & x_{L+1} & \cdots & \cdots & x_{N-1} \\ x_{L-2} & x_{L-1} & x_L & \cdots & \cdots & x_{N-2} \\ \vdots & \vdots & \vdots & \ddots & \cdots & \vdots \\ x_1 & x_2 & x_3 & \cdots & \cdots & x_{N-L+1} \end{bmatrix}_{L\ by\ N-L+1}. \tag{11}$$

Before detecting the fault features with MOMEDA, we should consider the solution targets of impulse trains and the solution is estimated as

$$t_n = P_n(T) = \delta_{round(T)} + \delta_{round(2T)} + \delta_{round(3T)} + ... \tag{12}$$

in which δ_n represents an impulse at sample n.

3.2 Simulated results

To examine the fact that MOMEDA is superior to MED, a

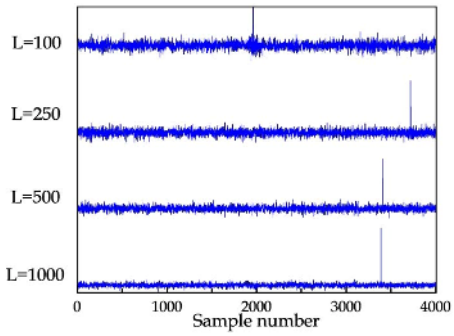

(a)

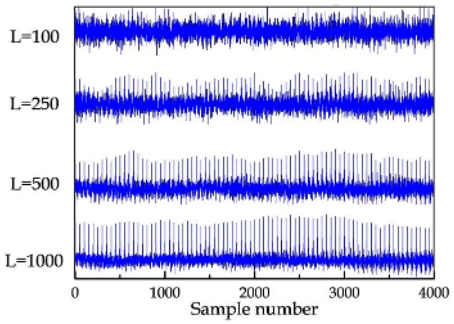

(b)

Fig. 3. (a) MED filtered output; (b) MOMEDA filtered output.

simulated fault signal is used here. In this simulation, the period of a fault impulse is 50, i.e., T = 50. Fig. 2 shows a simulated fault signal.

Different filter lengths L are selected to compare in this case since the filter length L produces a great influence on the kurtosis value of the output signals. As mentioned, MED is an iterative method, so the termination number of iterations is selected to be 30. The different results for MED versus MOMEDA are plotted in Fig. 3. As expected, MED can only detect a single impulsive component in each case, while the MOMEDA tool is can extract the multiple impulses.

4. Synthetic fault signal analysis

To examine the performance of the proposed approach, two cases using simulation data of faulty bearings are given here. The mathematical expression is

$$y(t)=\sum_{i=1}^{m}A_m e^{-\alpha\left(t-mT_p-\tau_i\right)}\cos\omega_r\left(t-mT_p-\tau_i+\theta_m\right) u\left(t-mT_p-\tau_i\right) \tag{13}$$

in which the mth impulse is A_m = 1; the damping coefficient is α = 1500 N s/m; the period is T = 0.01 s, and thus the corresponding fault characteristic frequency is f_{oc} = 100 Hz; the ω_r represents the excited resonance frequency and is set at ω_r = 2048 Hz . The sampling frequency is f_s = 12000 Hz. The period of the fault signal is equal to 120 by using Eq. (12). The flowchart of the proposed approach is presented in Fig. 4.

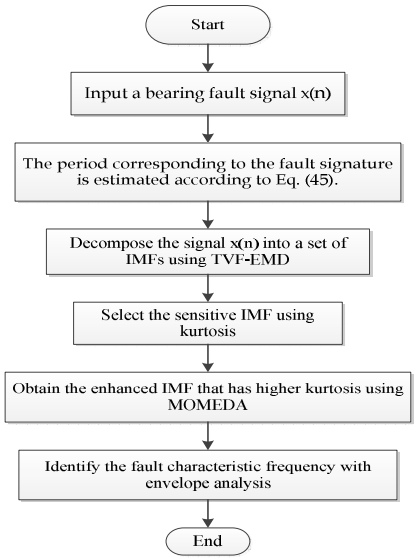

Fig. 4. The flowchart of the proposed approach.

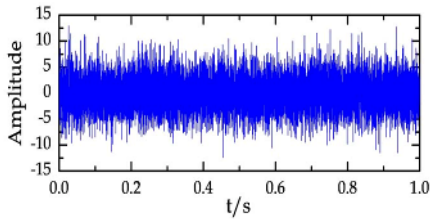

(a)

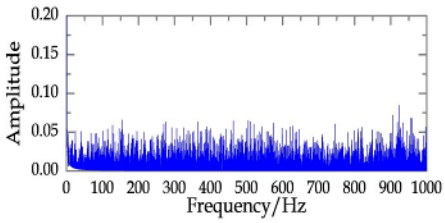

(b)

Fig. 5. (a) Mixed-signal; (b) Fourier spectrum.

4.1 Case 1- A synthetic fault vibration signal with a large magnitude of noise

In this case, additional Gaussian noise (SNR = -10 dB) is mixed in this synthetic bearing fault signal. The mixed signal and Fourier spectrum are displayed in Fig. 5. As one can see, no obvious impulses can be identified in the waveform and meanwhile, the intensive background noise dominates the frequency spectrum.

Now, TVF-EMD decomposes the mixed signal into 14 IMFs, and the first three IMFs are used to be further analyzed. These IMFs are illustrated in Fig. 6. According to the kurtosis values, we can find that the 3rd IMF is the sensitive IMF. As mentioned, the parameter of the filter length L in MOMEDA has to be predetermined. Here, we considered the values in the

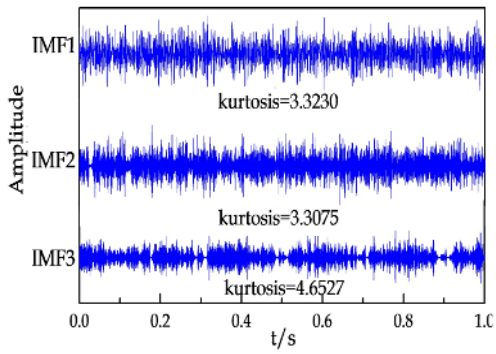

Fig. 6. IMFs.

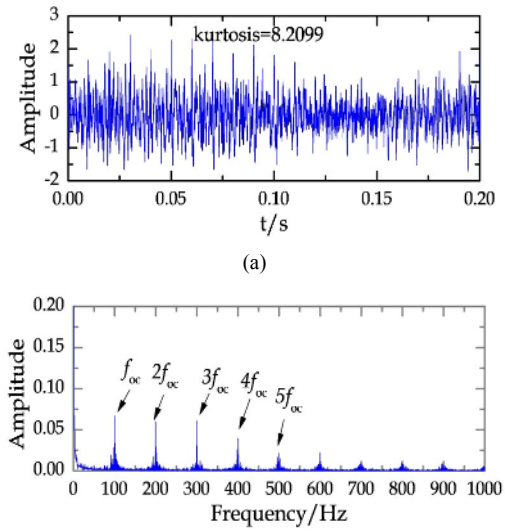

Fig. 7. (a) MOMEDA purified signal; (b) associated envelope spectrum.

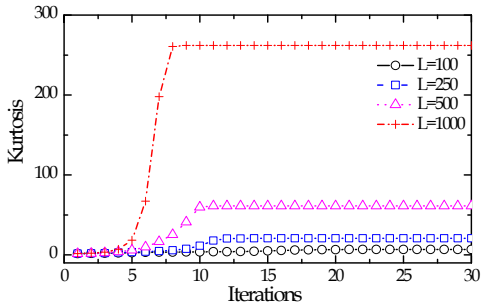

Fig. 8. Convergence of MED method.

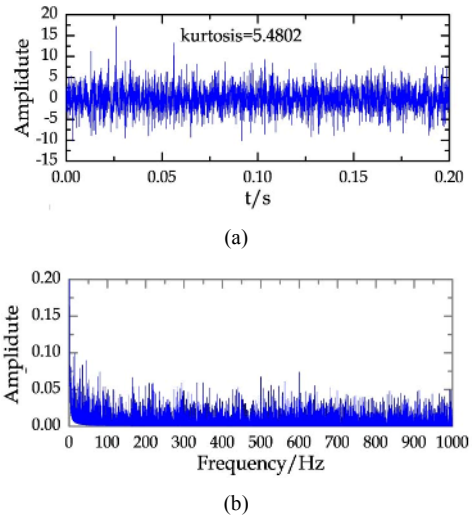

Fig. 9. (a) MED purified signal; (b) envelope spectrum.

case of $L \geq T$ (period) that the author recommended in Ref. [26]. Thus, L is set to be 1000 here. Then, the sensitive IMF is filtered by MOMEDA. Fig. 7 shows the part of the filtered IMF3 and its envelope spectrum. We can clearly see that the kurtosis value rises rapidly and the impulsive components are very obvious. Besides, the bearing fault characteristic frequency and its associated harmonics with obvious peaks can be detected in Fig. 7(b).

For comparison, the IMF3 is filtered by MED. Similar to MOMEDA, some user-defined parameters are also needed to be set. However, unlike MOMEDA, another important consideration in MED is the termination number of iterations which is also sensitive to the impulses except for the filter length L. Fig. 8 presents the convergence relationship of the kurtosis over the termination number of iterations. The convergence of characteristic of MED with four filter lengths (100, 250, 500 and 1000) are compared with each other.

Clearly, the convergence properties of MED are very different in the case of different filter lengths L and the termination number of iterations. Therefore, the selection of the two important parameters largely determines the performance of MED. Here, the filter lengths L and the termination number of iterations are selected to be 1000 and 10, respectively. As detailed in Fig 9, although the kurtosis value increases, the noise dominates the envelope spectrum and the simulated bearing fault characteristic frequency cannot be recognized.

To better present the superiority of the proposed approach, it is also employed to compare with the MOMEDA+envelop analysis and TVF-EMD+envelop analysis methods. We can find from Fig. 10(a) that the simulated bearing fault characteristic frequency at 100 Hz is almost masked by the heavy noise and its some harmonics such as $3f_{oc}$, $4f_{oc}$ and $5f_{oc}$ are unrecognizable. When investigating the result obtained by the "MOMEDA+envelop analysis" method in Fig. 10(b), the result is fully acceptable since the simulated bearing fault characteristic frequency and relevant harmonics can be clearly distinguished in the envelope spectrum. Nevertheless, when comparing with the result in Fig. 7(b), we can obviously see that the result yielded by the proposed approach is more satisfactory as the simulated bearing fault characteristic frequency and its associated harmonics have more remarkable peaks in Fig. 10(b).

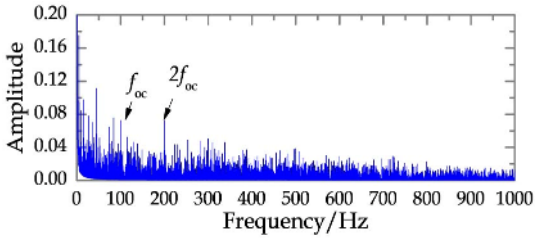

(a)

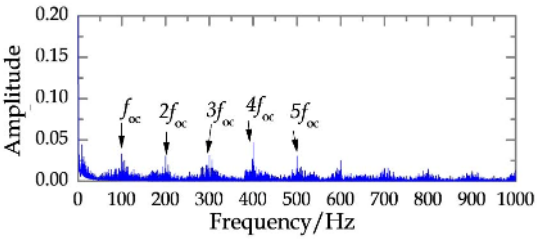

(b)

Fig. 10. (a) Result produced by the TVF-EMD+envelop analysis method; (b) result produced by the MOMEDA+envelop analysis method.

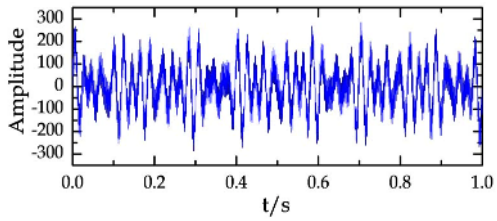

(a)

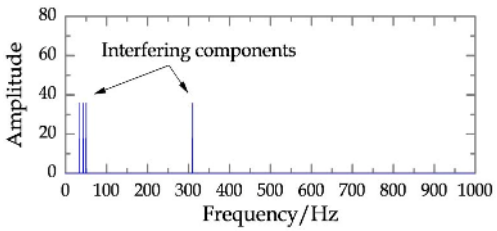

(b)

Fig. 11. (a) Mixed-signal; (b) Fourier spectrum.

4.2 Case 2- A synthetic bearing vibration signal with a large magnitude of noise and interfering components

In this case, a more complex synthetic fault signal with a large magnitude of noise and interfering components is employed. Fig. 11 shows the complex synthetic signal and its Fourier spectrum. Likewise, the signal including the impulsive information cannot be identified in Fig. 11(a) and only the interfering components exist in the frequency spectrum, yet not including the information about defects.

Subsequently, the synthetic fault signal is decomposed into 6 IMFs by TVF-EMD. The first five IMFs are illustrated in Fig. 12. Obviously, the 2nd IMF is suitable for further analysis. The 2nd IMF is then filtered by MOMEDA and the filtered

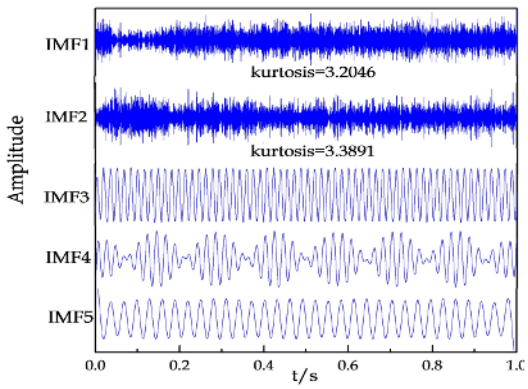

Fig. 12. IMFs.

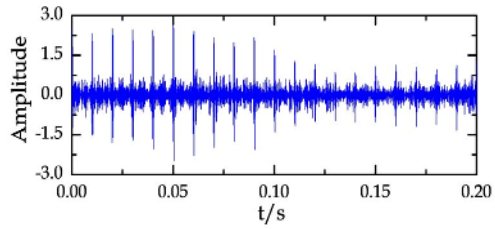

(a)

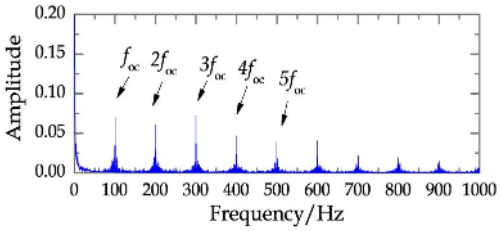

(b)

Fig. 13. (a) MOMEDA purified signal; (b) envelope spectrum.

result, as well as the envelope spectrum, are displayed in Fig. 13.

The simulated bearing fault characteristic frequency and its associated harmonics clearly dominate the envelope spectrum.

As before, using the MED method and envelope analysis to analyze the same synthetic fault signal yields the result in Fig. 14. Similar to the result in Fig. 9, MED-based method cannot extract the simulated bearing fault characteristic frequency and its relevant harmonics.

Finally, resembling case 1 previously, we also used the MOMEDA+envelop analysis and TVF-EMD+envelop analysis methods to compare with the proposed approach. The results produced by the two methods are displayed in Fig. 15 in which the TVF-EMD+envelop analysis method produces an unacceptable result under this environment as the simulated bearing fault characteristic frequency is fully obscured by noise. On the contrary, the MOMEDA+envelop analysis method succeeds in detecting the simulated bearing fault characteristic frequency and its associated harmonics, but the result is similar to that in Fig. 10(b). Thus, the simulated bearing fault characteristic frequency and its associated

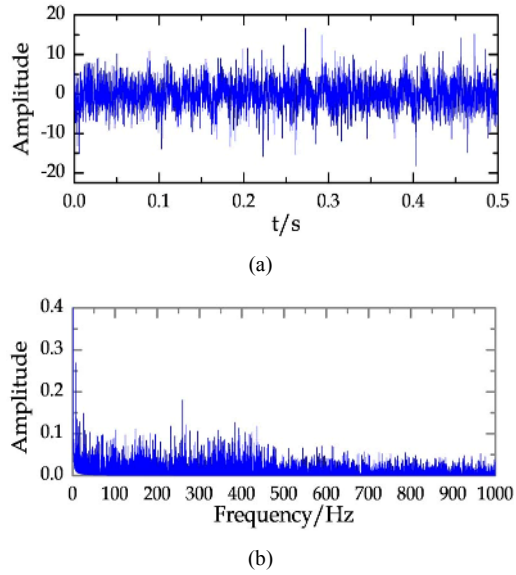

Fig. 14. (a) MED purified signal; (b) envelope spectrum.

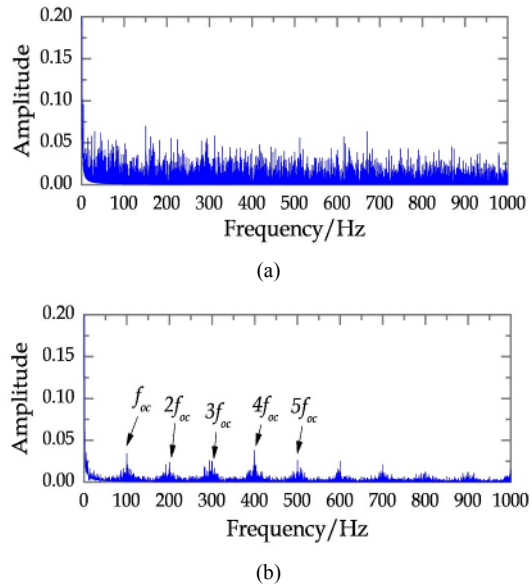

Fig. 15. (a) Result produced by the TVF-EMD+envelop analysis method; (b) result produced by the MOMEDA+envelop analysis method.

harmonics in Fig. 15(b) are at lower amplitudes in comparison with those in Fig. 13(b).

According to the previous tests, it is apparent that in all cases the proposed method not only succeeds in extracting the simulated bearing fault characteristic frequency and multiple harmonics, but also they are all at a higher amplitude and easily recognizable. In contrast to the MOMEDA technique, applying the MED technique and envelope analysis to the sensitive IMF decomposed by TVF-EMD gives rise to unsatisfactory results. For the TVF-EMD+envelop analysis method, its fault detection performance is not always reliable since it fails to detect the fault signature in case 2. We can see

Table 1. Specifications of the bearing.

Ball diameter (mm)	Pitch circle diameter (mm)	No. of rolling elements	Contact angle
7.12	38.5	12	0°

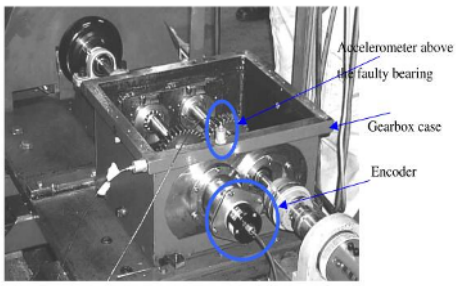

Fig. 16. Spur gear rig [30].

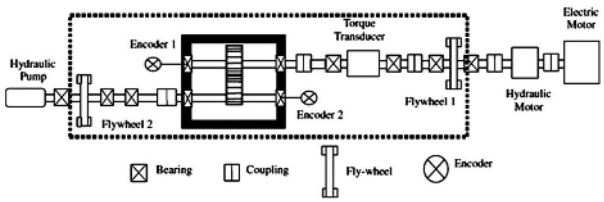

Fig. 17. Schematic diagram of this spur gearbox [30].

from the comparison results that the performance of the MOMEDA+envelop analysis approach is closely similar to the that of the proposed method, but its performance is less than perfect due to the lower amplitudes of the fault frequency. In addition, from the results in Figs. 7(b) and 13(b) the proposed method is almost unaffected when the working condition becomes tougher. Consequently, the proposed method outperforms the MED-based and mode decomposition-based methods.

5. Case study

To verify the usefulness and effectiveness of the proposed approach, it is applied to the real vibration signals in this section.

5.1 Experimental set-up

In real experiments, the bearing fault data provided by the University of New South Wales (UNSW) was used in this study [20, 30]. The bearing fault signals were extracted from a spur gearbox test rig, as shown in Fig. 16. The schematic diagram of the spur gearbox is given in Fig. 17.

The speed of the output shaft was approximately set to 6 Hz (360 rpm) for all signals. The sampling frequency of these signals was 48000 sample/s (48 kHz). The specifications of the bearing used in the tests are listed in Table 1:

The fault characteristic frequencies related to the bearing are listed in Table 2.

Note that between the estimated fault characteristic

Table 2. Fault characteristic frequencies.

Positions	Value (Hz)
Outer ring (BPFO)	29.34
Inner ring (BPFI)	42.66
Rolling element (BSF)	15.67

Table 3. Estimated periods.

Positions of fault signatures	Value
Outer ring	1636
Inner ring	1125
Rolling element	3063

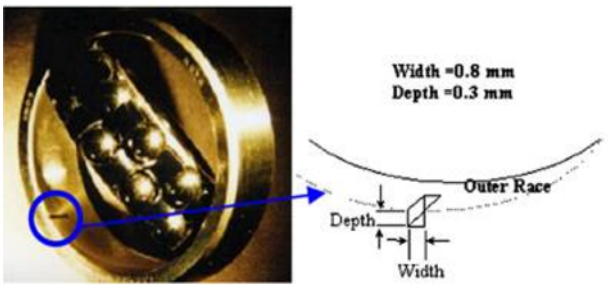

Fig. 18. Outer ring defect [30].

frequency and measured fault characteristic frequency, there is an error by a small percentage s that is typical of the order 1-2 % owing to slip [20]. Then, the periods corresponding to three types of fault signatures were calculated, as detailed in Table 3.

5.2 Fault diagnosis of the outer ring

Fig. 18 displays the details of the outer ring defect. It can be seen that a notch is machined into the outer ring of the bearing. The width and depth of the outer ring defect are displayed in Fig. 18.

Fig. 19 illustrates the acceleration signal of the outer ring defect and its corresponding Fourier spectrum. We can find that the fault impulsive components fail to be seen from the acceleration signal and the fault characteristic frequency at 29.34 Hz fails to be distinguished, and only the gear meshing frequency and its associated harmonics are dominant in the Fourier spectrum.

Likewise, TVF-EMD first decomposes the outer race fault signal into 5 IMFs. Fig. 20 displays the time domain of the 5 IMFs and their corresponding values of the kurtosis.

The 2nd IMF is a sensitive IMF as it has a considerable kurtosis. As before, to start with, the filter length has to be predetermined. Fig. 21 illustrates the variation characteristic of the kurtosis over the different filter lengths *L*. It can be found that the values of the kurtosis of different filter lengths (L = 2000, 2500, 3000, 3500 and 4000) remain constant approximately, so the filter length *L* is set to be 3000.

Next, the 2nd IMF is enhanced by MOMEDA. The enhanced signal and its corresponding envelope spectrum are

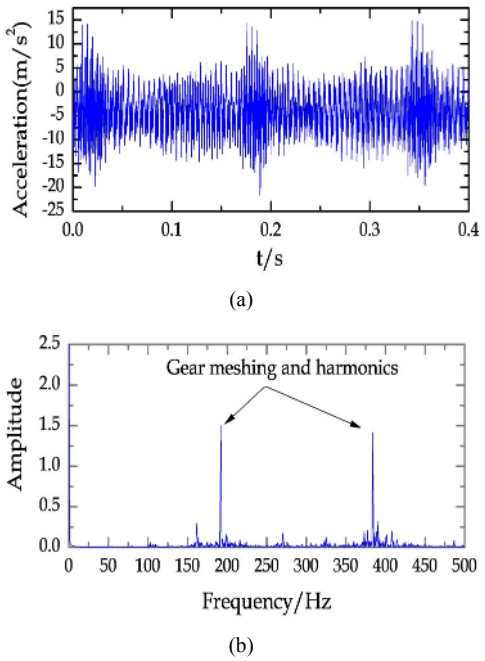

Fig. 19. (a) Acceleration signal; (b) Fourier spectrum.

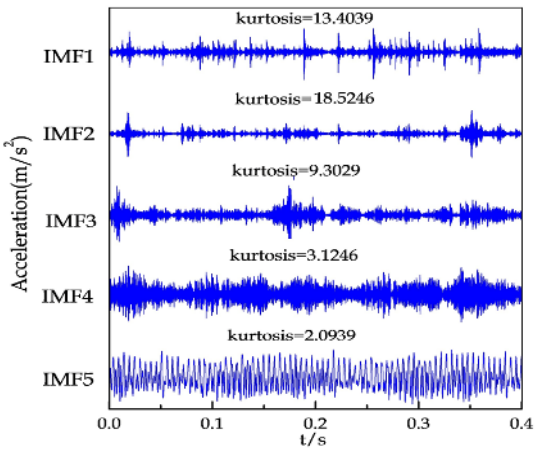

Fig. 20. IMFs decomposed by TVF-EMD.

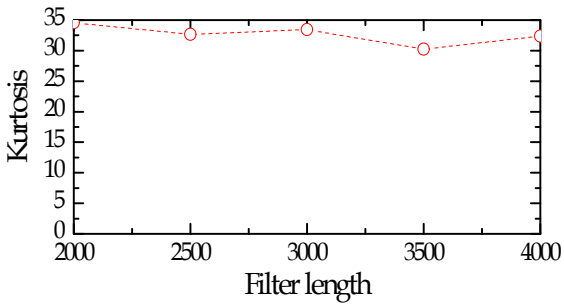

Fig. 21. Variation characteristic of the kurtosis.

shown in Fig. 22. The fault impulse train is obviously extracted by MOMEDA and meanwhile, the value of the kurtosis of the enhanced signal is much greater than that of the original 2nd IMF. In Fig. 22(b), the fault characteristic

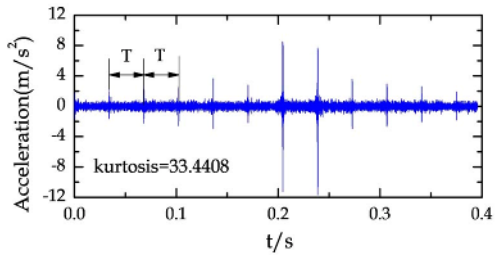

(a)

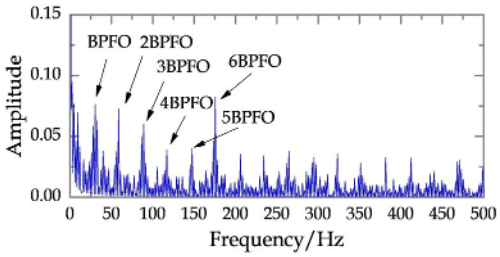

(b)

Fig. 22. (a) Enhanced signal; (b) envelope spectrum.

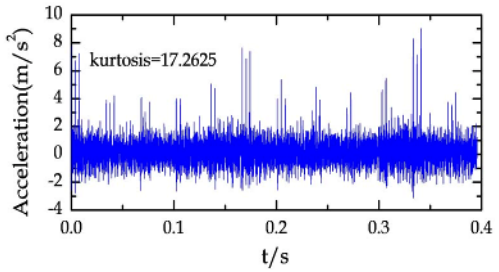

(a)

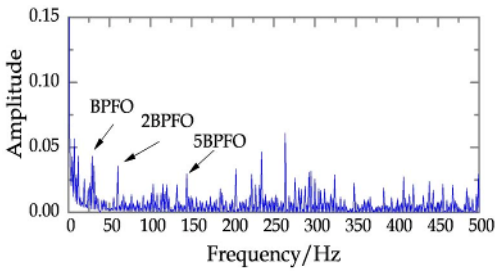

(b)

Fig. 23. (a) Directly enhanced signal; (b) envelope spectrum.

frequency and its multiple harmonics can be also identified clearly.

For comparison, the measured signal is directly enhanced by MOMEDA and pre-processing using TVF-EMD is omitted. The directly enhanced signal and its corresponding envelope spectrum are illustrated in Fig. 23. The kurtosis value of the directly enhanced signal is obviously much smaller and the fault characteristic frequency at 29.34 Hz can be detected, but some harmonics (3BPFO and 4BPFO) disappear as shown in Fig. 23(b). Furthermore, the amplitudes of the fault characteristic frequency and its relevant harmonics are smaller

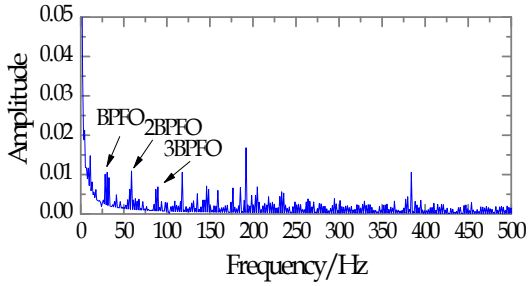

Fig. 24. Envelope spectrum of the 2nd IMF.

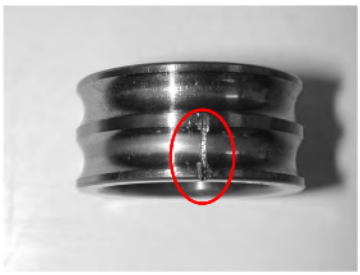

Fig. 25. Inner ring defect.

in comparison with the result in Fig. 22(b). Accordingly, the result in Fig. 23(b) is acceptable grudgingly but not very satisfactory.

Finally, the TVF-EMD+envelope analysis method is employed to compare with the proposed approach. Fig. 24 displays the envelope spectrum of the 2nd IMF. Similar to the result in Fig. 23(b), the outer ring fault characteristic frequency and its some harmonics are extracted, but their amplitudes are very small and some harmonics are not easily recognizable.

5.3 Fault diagnosis of the inner ring

The dimensions of the inner ring defect are in line with those of the outer ring defect. Fig. 25 displays the inner ring defect.

The acceleration signal of the inner race with a notch and its corresponding Fourier spectrum are illustrated in Fig. 26. As before, the fault impulse train cannot be observed from the acceleration signal and the fault characteristic frequency at 42.66 Hz fails to also be detected in the frequency spectrum.

Similar to the previous test, we first apply the TVF-EMD method to decompose the raw signal. This time TVF-EMD decomposes the raw signal into 6 IMFs. The time domain waveforms of the 6 IMFs are shown in Fig. 27.

According to the values of the kurtosis in Fig. 27, the 1st IMF is selected to be further processed by MOMEDA. Similarly, we first determine a filter length L that is larger than the fault period T. Fig. 28 shows the relationship between the kurtosis values and the filter length. Unlike the result of Fig. 20, only the values of the kurtosis in the case of L = 2000 and L = 2500 are greater than that of the 1st IMF and therefore the filter length is selected to be 2500.

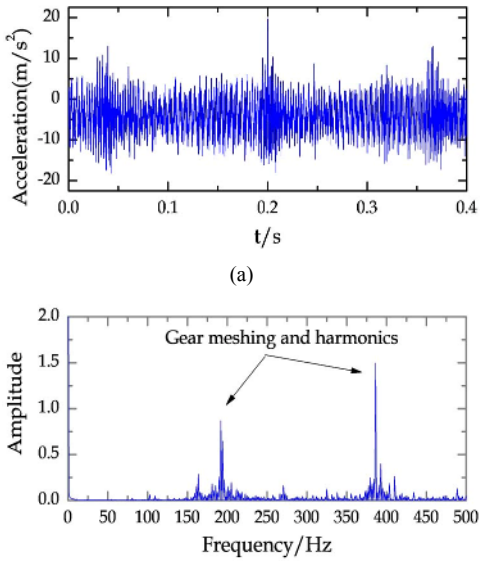

Fig. 26. (a) Measured signal; (b) Fourier spectrum.

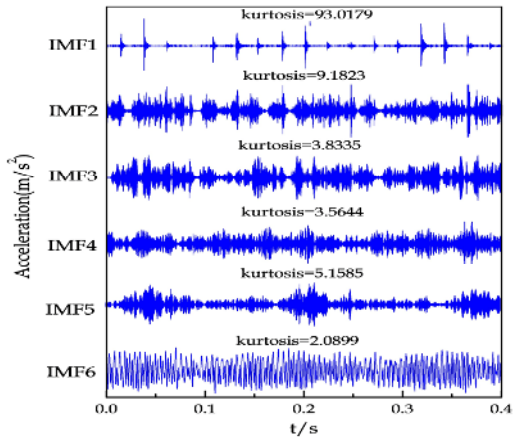

Fig. 27. IMFs decomposed by TVF-EMD.

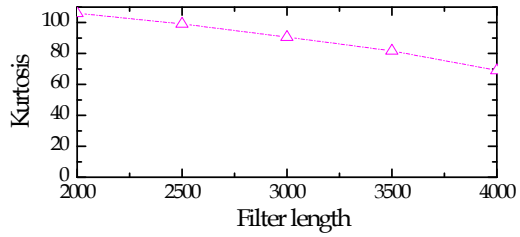

Fig. 28. Variation characteristic of the kurtosis.

Fig. 29 displays the fault impulse train extracted by MOMEDA and its envelope spectrum. As we can see in Fig. 29(a), the value of the kurtosis is just a little bigger than that of the 1st IMF. The inner ring fault characteristic frequency and eleven of its harmonics can be clearly observed in the envelope spectrum after applying the MOMEDA technique.

For the sake of comparing with the proposed approach, the

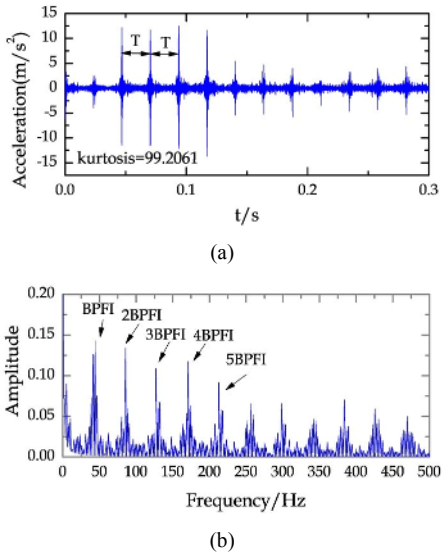

Fig. 29. (a) Enhanced signal; (b) its envelope spectrum.

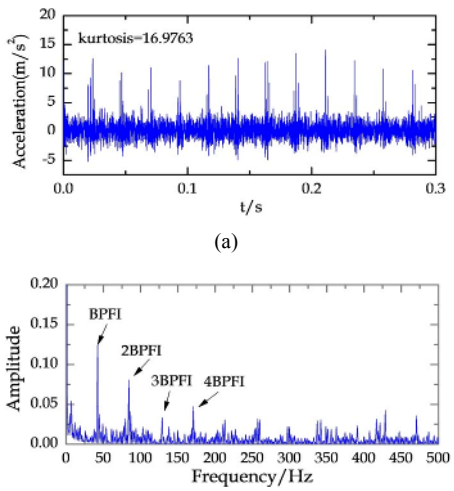

Fig. 30. (a) Directly enhanced signal; (b) envelope spectrum.

raw signal is directly subjected to the MOMEDA method as before. The extracted fault impulse train and the result of the envelope are presented in Fig. 30. As indicated in Fig. 30, using the approach described above, the extraction result of the inner race fault is obviously superior to that of the outer race fault. It is found that there is a more obvious peak at the fault characteristic frequency. Despite this, compared to the proposed method, some of the associated harmonics in the envelope spectrum are still difficult to recognize due to the lower amplitudes.

Finally, similar to the experiment above, the 1st IMF is directly analyzed by envelope analysis. The result of the envelope is shown in Fig. 31. We can observe from Fig. 31 that, in this case, this TVF-EMD+envelope analysis method produces a satisfactory result which is identical to the result of the proposed approach. However, one is likely to prefer the

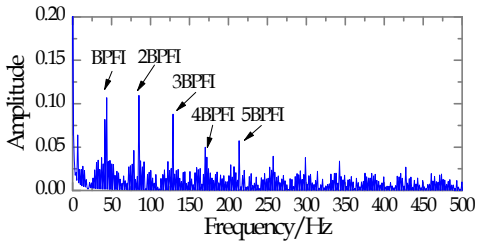

Fig. 31. Envelope spectrum of the 1st IMF.

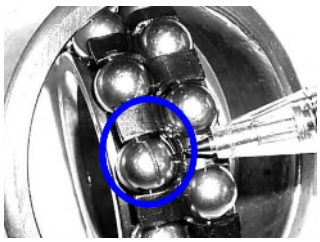

Fig. 32. Rolling element fault.

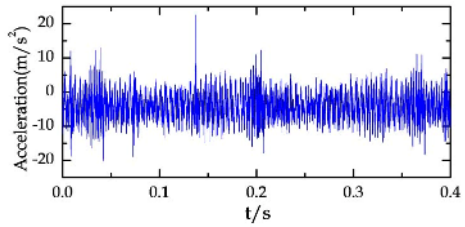

(a)

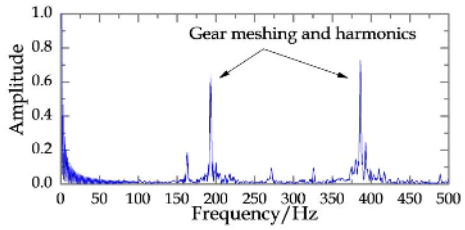

(b)

Fig. 33. (a) Acceleration signal; (b) Fourier spectrum.

strength of the proposed approach in consideration that the proposed approach succeeds in detecting the fault characteristic fault at a high amplitude with more discernible harmonics.

5.4 Fault diagnosis of rolling element

The generated gap that had a rectangular cross-section is displayed in Fig. 32. The depth and width of the gap are both set to be 0.5 mm.

Fig. 33 shows the measured accelerometer signal of the rolling element defect and its corresponding Fourier spectrum. Similar to the previous tests, there are no signal components featuring impulsive signatures in the acceleration time signal and we cannot also observe the rolling element fault characteristic frequency in the frequency spectrum. Only the

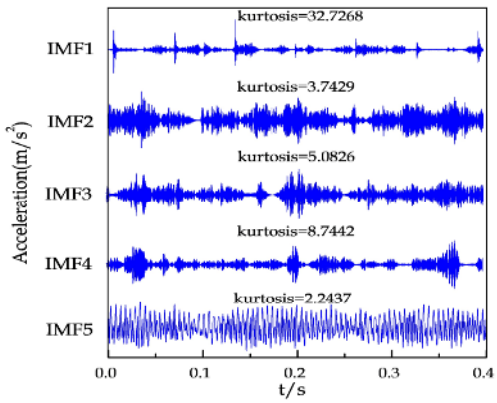

Fig. 34. IMFs derived by TVF-EMD.

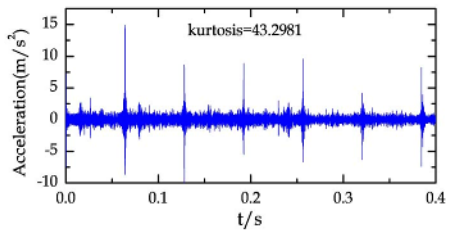

(a)

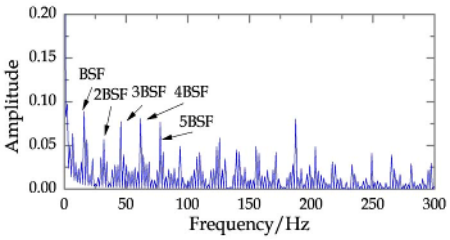

(b)

Fig. 35. (a) Enhanced signal; (b) envelope spectrum.

frequency components related to the gearing meshing and its harmonics dominate the Fourier spectrum of the acceleration signal.

Now, similarly, TVF-EMD decomposes the acceleration signal into 5 IMFs. The obtained 5 IMFs are displayed in Fig. 34.

As detailed in Fig. 34, the 1st IMF that has the greatest value of the kurtosis is selected for further analysis. Then, we apply the MOMEDA technique to the 1st IMF. Here, the length filter L is selected to be 4000. The filtered signal including the obvious impulses and envelope spectrum are shown in Fig. 35. As one can see from Fig. 35, the fault impulses obviously exist in the enhanced signal and the rolling element fault characteristic frequency at 15.67 Hz, and some of harmonics at 31.34 Hz, 47.01 Hz, 62.68 Hz and 78.35 Hz can be clearly distinguished from the result.

The same as the previous experiments, to compare the result in Fig. 35 with those of the other two methods, the raw signal is directly subjected to the MOMEDA technique. The directly filtered signal and its corresponding envelope spectrum are

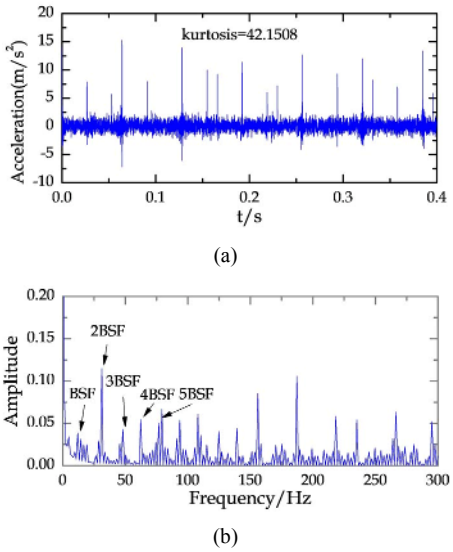

Fig. 36. (a) Directly enhanced signal; (b) envelope spectrum.

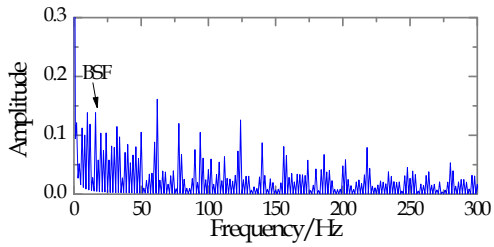

Fig. 37. Envelope spectrum of the 1st IMF.

illustrated in Fig. 36. It is found from Fig. 36(a) that the harmonics of the fault signature have obvious peaks that are easily recognized, but the fault characteristic frequency at 15.67 Hz is at a lower amplitude in contrast with the result of the proposed method. Hence, like the case of the detection of the outer ring fault characteristic frequency, the result is not incompletely satisfactory if the fault signal is directly filtered by the MOMEDA technique.

Finally, Fig. 37 presents the envelope spectrum of the 1st IMF unfiltered by MOMEDA. The fault characteristic frequency at 15.67 Hz and its the first two harmonics at 31.34 Hz and 47.01 Hz are almost masked by noise and other vibration components, which means that this method is not an ideal way to identify the rolling element fault characteristic frequency.

Through the real experimental results, it can be found that in the test for inner ring fault detection, the performance of the two methods used for comparison is similar to that of the proposed approach, but as the simulated results presented above, the other two methods are not always workable in the whole real tests. Their performance would be affected by the change of the fault location. However, the performance of the proposed approach is always stable. Thus, on the whole, the proposed method evidently outperforms the other two methods.

6. Conclusions

A wealth of well-understood methods and algorithms used in detecting the weak bearing fault signature have been proposed recently, yet some of the problems in bearing fault diagnosis still remain unanswered. Thus, an alternative approach based on TVF-EMD and MOMEDA is proposed to extract the bearing fault features in this paper. Unlike other pre-filtering techniques, the TVF-EMD can decompose a vibration signal into a group of IMFs with physical meanings and meantime adaptively, separate the background noise and vibration interferences from the vibration signal, which prepares for the further analysis. Then MOMEDA is used to highlight the impulsive components, which can lead to more effective bearing fault identification. The envelope analysis reveals the fault characteristic frequency and relevant harmonics in the last step.

Overall, the findings of this work are presented as follows:

(1) The proposed approach requires little prior knowledge about the mechanical system, and only the length filter L is needed to be predefined. Generally, this parameter is easy to determine, i.e., $L \geq T$.

(2) The experimental results provide compelling evidence that the proposed approach can successfully detect fault characteristic frequencies of any component of a bearing under the harsh working condition. Besides, the proposed method outperforms some previous methods according to the experimental comparisons.

(3) Moreover, it may also provide an alternative to fault diagnosis and fault features extraction of other mechanical elements, such as gear fault diagnosis.

However, the index of selecting the filter length L only by kurtosis may not be an optimal solution, although kurtosis is recommended in numerous studies. Accordingly, it would be beneficial to provide an approach to obtain the optimal solution for the parameter of length filter in a future study.

Acknowledgments

The authors thank Prof. Bob Randall for providing the bearing fault data freely in his published book. This work is supported by the Fundamental Research Funds for the Central Universities, CHD (No. 300102258714 and 30010223801), the National Natural Science Foundation of China (No. 51705030), and the Special Funds for Education and Teaching reform for the Central Universities (No. 310625176501).

References

[1] K. F. Al-Raheem et al., Rolling element bearing faults diagnosis based on autocorrelation of optimized: Wavelet de-noising technique, *International J. of Advanced Manufacturing Technology,* 40 (3-4) (2009) 393-402.

[2] H. Qiu, J. Lee, J. Lin and G. Yu, Wavelet filter-based weak signature detection method and its application on rolling

element bearing prognostics, *J. of Sound and Vibration,* 289 (4) (2006) 1066-1090.

[3] A. Djebala, N. Ouelaa and N. Hamzaoui, Detection of rolling bearing defects using discrete wavelet analysis, *Meccanica,* 43 (3) (2008) 339-348.

[4] H. Zhao et al., Study on a novel fault damage degree identification method using high-order differential mathematical morphology gradient spectrum entropy, *Entropy,* 20 (9) (2018) 1-18.

[5] B. Eftekharnejad, M. R. Carrasco, B. Charnley and D, Mba, The application of spectral kurtosis on Acoustic Emission and vibrations from a defective bearing, *Mechanical Systems and Signal Processing,* 25 (1) (2011) 266-284.

[6] J. Xiang, Y. Zhong and H. Gao, Rolling element bearing fault detection using PPCA and spectral kurtosis, *Measurement,* 75 (2015) 180-191.

[7] S. Jin, J. S. Kim and S. K. Lee, Sensitive method for detecting tooth faults in gearboxes based on wavelet denoising and empirical mode decomposition, *J. of Mechanical Science and Technology,* 29 (8) (2015) 3165-3173.

[8] W. Deng et al., A novel fault diagnosis method based on integrating empirical wavelet transform and fuzzy entropy for motor bearing, *IEEE Access,* 6 (2018) 35042-35056.

[9] S. Jin and S.-K. Lee, Bearing fault detection utilizing group delay and the Hilbert-Huang transform, *J. of Mechanical Science and Technology*, 31 (3) (2017) 1089-1096.

[10] Q. Xiong, Y. Xu, Y. Peng, W. Zhang, Y. Li and L. Tang, Low-speed rolling bearing fault diagnosis based on EMD denoising and parameter estimate with alpha stable distribution, *J. of Mechanical Science and Technology*, 31 (4) (2017) 1587-1601.

[11] Y. Guo, J. Na, B. Li and R.-F. Fung, Envelope extraction based dimension reduction for independent component analysis in fault diagnosis of rolling element bearing, *J. of Sound and Vibration,* 333 (13) (2014) 2983-2994.

[12] L. Han, C. W. Li, S. L. Guo and X. W. Su, Feature extraction method of bearing AE signal based on improved FAST-ICA and wavelet packet energy, *Mechanical Systems and Signal Processing,* 62 (2015) 91-99.

[13] W. Deng et al., A novel intelligent diagnosis method using optimal LS-SVM with improved PSO algorithm, *Soft Comput.* (2017) 1-18.

[14] T. Yang, H. Pen, Z. Wang and C. S. Chang, Feature knowledge based fault detection of induction motors through the analysis of stator current data, *IEEE Transactions on Instrumentation and Measurement,* 65 (3) (2016) 49-558.

[15] W. Deng et al., A novel collaborative optimization algorithm in solving complex optimization problems, *Soft Comput.,* 21 (15) (2017) 4387-4398.

[16] Y. Lei, F. Jia, J. Lin, S. Xing and S. X. Ding, An intelligent fault diagnosis method using unsupervised feature learning towards mechanical big data, *IEEE Transactions on Industrial Electronics*, 63 (5) (2016) 3137-3147.

[17] W. Deng et al., Study on an improved adaptive PSO algorithm for solving multi-objective gate assignment, *Appl. Soft Comput. J.,* 59 (2017) 288-302.

[18] T. Han, D. Jiang, Y. Sun, N. Wang and Y. Yang, Intelligent fault diagnosis method for rotating machinery via dictionary learning and sparse representation-based classification, *Measurement,* 99 (2018) 459-477.

[19] Z. Wang, Z. Han, F. Gu, J. X. Gu and S. Ning, A novel procedure for diagnosing multiple faults in rotating machinery, *ISA Transaction,* 55 (2015) 208-218.

[20] R. B. Randall, *Vibration-based Condition Monitoring: Industrial, Aerospace and Automotive Applications*, Wiley (2010).

[21] R. A. Wiggins, Minimum entropy deconvolution, *Geoexploration,* 16 (1) (1978) 21-35.

[22] H. Endo and R. B. Randall, Enhancement of autoregressive model based gear tooth fault detection technique by the use of minimum entropy deconvolution filter, *Mechanical Systems and Signal Processing,* 21 (2007) 906-919.

[23] Q. Li, X. Ji and S. Y. Liang, Incipient fault feature extraction for rotating machinery based on improved AR-minimum entropy deconvolution combined with variational mode decomposition approach, *Entropy,* 19 (7) (2017) 317.

[24] R. Jiang, J. Chen, G. Dong, T. Liu and W. Xiao, The weak fault diagnosis and condition monitoring of rolling element bearing using minimum entropy deconvolution and envelop spectrum, *Proceedings of the Institution of Mechanical Engineers, Part C: J. of Mechanical Engineering Science,* 227 (5) (2013) 1116-1129.

[25] N. Sawalhi, R. B. Randall and H. Endo, The enhancement of fault detection and diagnosis in rolling element bearings using minimum entropy deconvolution combined with spectral kurtosis, *Mechanical Systems and Signal Processing,* 21 (6) (2007) 2616-2633.

[26] G. L. McDonald and Q. Zhao, Multipoint optimal minimum entropy deconvolution and convolution fix: Application to vibration fault detection, *Mechanical Systems and Signal Processing,* 82 (2017) 461-477.

[27] Z. Wang, J. Wang, Z. Zhao and R. Wang, A novel method for multi-fault feature extraction of a gearbox under strong background noise, *Entropy,* 20 (1) (2018) 10.

[28] H. Li, Z. Li and W. Mo, A time varying filter approach for empirical mode decomposition, *Signal Processing,* 138 (2017) 146-158.

[29] N. E. Huang, Z. Wu, S. R. Long, K. C. Arnold, X. Chen and K. Blank, On instantaneous frequency, *Advances in Adaptive Data Analysis,* 1 (2) (2009) 177-229.

[30] N. Sawalhi and R. B. Randall, Simulating gear and bearing interactions in the presence of faults. Part I. The combined gear bearing dynamic model and the simulation of localised bearing faults, *Mechanical Systems and Signal Processing,* 22 (8) (2008) 1924-1951.

[31] Y. Xu, Z. Cai and K. Ding, An enhanced bearing fault diagnosis method based on TVF-EMD and a high-order energy operator, *Measurement Science and Technology,* 29 (9) (2018) 095108.

Yuanbo Xu received a B.S. in Mechanical Engineering from Zhejiang SCI-TECH University, Hangzhou, China in 2009. He is currently a Ph.D. candidate at Chang' an University. His primary research interest is machine fault diagnosis.

Zongyan Cai is a Professor of Mechanical Engineering at Chang' an University. He received his Ph.D. from Northwestern Polytechnical University in China. His research interests include Intelligent robot technology, signal processing and Intelligent fault diagnosis.